Damage Nucleation During Transverse Creep of a Directionally Solidified Ni-based Superalloy

Jean Charles Stinville[a,1], Lorena Mataveli Suave[b,c], Florent Mauget[b], Lionel Marcin[d], Patrick Villechaise[b], Tresa M. Pollock[e], Jonathan Cormier[b,1]

[a] *University of Illinois at Urbana-Champaign, Urbana, USA*
[b] *Institut Pprime, UPR CNRS 3346, ISAE-ENSMA, BP 40109, Futuroscope-Chassenueil, Poitiers, France*
[c] *Safran Tech, Magny les Hameaux, France*
[d] *Safran Aircraft Engines, Moissy Cramayel, France*
[e] *Materials Department, University of California Santa Barbara, Santa Barbara, California, USA*

Abstract

A directionally solidified Ni-based superalloy DS200 is investigated under low (750°C) and high temperature (900°C) transverse creep. In-situ creep tests with strain measurements are performed to capture creep strain evolution in the individual crystallographic grains. Moreover, the microstructure configurations that promote damage nucleation are identified as a function of the loading condition. High angle grain boundaries are the preferred sites for crack nucleation under all investigated loading conditions. However, grain boundary configurations promoting crack nucleation are observed to significantly differ as a function of the loading conditions. Such observation is discussed in view of creep behavior and damage processes.

Keywords:
Transverse Creep, Directionally Solidified Ni-Based Superalloy, DS200, GTD444, crack nucleation

1. Introduction

Directionally solidified (DS) Ni-based superalloys are preferred materials for manufacturing blades, and vanes of hot sections of aeroengines and industrial gas turbines for power generation [1, 2, 3]. DS Ni-based superalloys usually have a columnar grain structure with their main grain axis closely aligned with the principal loading direction (i.e., centrifugal forces in the case of rotating components). In addition, the directional solidification process leads to the main grain axis usually close to a [001] crystallographic orientation, secondary orientations being random [2]. Consequently, most of the mechanical properties available in the literature regarding the durability of these DS alloys in creep or fatigue have been generated along the longitudinal direction (i.e., with the uniaxial loading direction aligned with the solidification direction) [4, 5, 6, 7, 8, 9, 10]. Limited data has been published on their mechanical properties along their transverse directions [11, 12, 13, 14, 15, 16, 17, 18]. Due to intricate internal cooling systems in blades and vanes, as well as complex thermo-mechanical loading paths, the local loading direction happens to be misoriented with respect to the solidification direction, leading to the necessity of characterizing the mechanical strength of this class of alloys along their transverse directions (transverse mechanical properties). Moreover, during service operations, shrouds of long blades are mainly loaded along transverse direction. Stinville et al. [11], Mataveli Suave et al. [13] and Kobayahsi et al. [19] have shown that intergranular fracture modes are observed during transverse creep and dwell-fatigue testing at high temperature. The observed intergranular fracture modes either originated from the local stress state nearby grain boundaries [11, 19] and/or from oxidation processes [13, 14]. However, the temperature and stress dependencies of the damage nucleation

*corresponding authors: jcstinv@illinois.edu (Jean-Charles Stinville), jonathan.cormier@ensma.fr (Jonathan Cormier).

processes are not yet identified. The present work elucidates the mechanisms leading to intergranular crack nucleation in DS Ni-based superalloys and their temperature and stress dependencies. In addition, the critical crystallographic configurations leading to intergranular crack nucleation are identified. A better understanding of the underlying mechanisms controlling the large variability in DS Ni-based superalloy creep life is provided.

2. Experimental procedures and Materials

2.1. Material

The Ni-based superalloys GTD444, DS200, and Mar-M200 are investigated in this study and present nominal chemical compositions reported in Table 1. The DS200 alloy is the directionally solidified version of the single crystal Mar-M200, and both of them display identical chemistry. The single crystal Mar-M200 alloy is used as a reference alloy. The DS200 and Mar-M200 superalloys show a substantial amount of hafnium. A high hafnium content prevents grain boundary hot tearing during processing and provides better grain boundary strengths at high-temperature [20]. All investigated alloys contain a level of carbon and boron that provide higher damage tolerance to high-angle boundaries during creep [21, 22, 23]. While the DS200 alloy displays a directionally solidified microstructure with several grains/boundaries across the gauge length, the GTD444 specimens are bicrystals, displaying a single grain boundary transverse to the loading direction. These three alloys and associated microstructures are used to investigate the grain boundary effect on creep properties of Ni-based superalloys.

Bicrystalline slabs of GTD444 alloy were solidified by the LMC method [24]. The liquid metal cooling container held a 500 kg Sn bath maintained at 250 °C and was combined with a dynamic, floating ceramic baffle. The 1.5-cm-thick baffle consisted of hollow and solid beads, each comprising zirconium silicate. Ingots of the superalloy were induction melted with a maximum temperature of 1550°C and poured into a pre-heated investment mold. Bicrystals were withdrawn at a rate of 8.5 mm/min. Double-seeded molds were used with seeds to achieve a single boundary of specific misorientation. The desired bicrystal boundary misorientation was achieved by rotating one seed relative to the other around its normal axis. The experimental details of this procedure are provided elsewhere [11].

The Ni-based superalloy DS200 specimens were machined from solution-treated plates that were directionally solidified. The solution heat treatment consisted of a plateau at 1210°C for 30 min, followed by a hold at 1225°C for 30 min and a final hold at 1240°C for 4 hours. The following cooling is done at 45°C/min until 700°C and air quench is performed. Plates were further heat-treated for 5 hours at 1100°C, followed by an air quench. The last heat treatment step consisted of a hold at 870°C for 16 hours, followed by an air quench to optimize the $\gamma\prime$ precipitate size and morphology. The experimental details of this procedure are provided elsewhere [13, 25]. The resulting microstructure of the DS200 specimen is presented in Figure 1. Examination of the specimens surface reveals equiaxed grains with highly serrated grain boundaries in a plane perpendicular to the solidification direction. Hf-rich carbides with average size of 5 µm are observed in Figure 1(b). γ-$\gamma\prime$ eutectic pools are also present in the material as shown in Figure 1(c). The $\gamma\prime$ precipitates in the fully heat-treated state were measured to in the range of 350 and 400 nm.

2.2. Fractorgraphy and microstructural inspections

An FEI XL 30 scanning electron microscope equipped with an electron backscatter diffraction (EBSD) TSL OIM system was used to examine fracture surfaces, specimens surfaces, and crystallographic orientation. Diffraction patterns for EBSD measurement were acquired using the EDAX OIM-Hikary XM4 EBSD detector, with an accelerating voltage of 20 kV, a 4×4 binning, and a beam current of about 0.2 nA.

2.3. Conventional Creep tests

DS200 creep specimens with total length of 42 mm, gauge length of 14 mm and gauge diameter of 4 mm were tested. Gauge lengths were mechanically polished up to a 4000 grade SiC paper, with final polishing along the longitudinal direction. Creep specimens were tested at 750°C and 800 MPa, 900°C and 250 MPa, 900°C and 300 MPa, 900°C and 350 MPa and 900°C and 400 MPa. The tests were performed using a creep

machine equipped with a laser extensometer. Heating was ensured with a radiant furnace. The experimental details of this procedure are provided elsewhere [26]. DS200 specimens were machined from solution-treated plates along the transverse and longitudinal directions. Typical transverse and longitudinal microstructures along the gauge length of the specimens are presented in Figure 2(a and b).

Single crystals Mar-M200 along the <001> direction were also solidified with identical processing parameters to the DS200 specimens. The creep specimens of Mar-M200 were machined along the solidification direction. Consequently, the Mar-M200 creep specimens display a single grain with a <001>-orientation along the loading direction as shown in Figure 2(c).

GTD444 tensile creep specimens with a gauge length of 24.7 mm and gauge diameter of 3 mm were machined from the GTD444 slabs along the transverse direction. The bicrystal boundary is located in the center of the gauge length and perpendicular to the loading direction. The procedure can be found elsewhere [11]. Typical microstructure along the gauge length of a GTD444 specimen is presented in Figure 2(d).

2.4. Creep tests with strain markers

Specimens with flat surfaces and a thickness of 1.5 mm were machined from cylindrical DS200 specimens by electrical discharge machining. After surface polishing up to a 4000 grade SiC paper, chemical etching revealed grain structure. One to three grains are reported across the width and thickness of the specimens, while more than ten grains are observed along the gauge length. Ceramic markers were placed in each crystallographic grain to measure local displacement by video-extensometry as shown in Figure 3. These markers were deposited by hand with a specific tool under optical microscope. These markers were then dried at ambient temperature for one night before testing. EBSD measurements were performed before strain markers deposition. S-type thermocouples used to control temperature during creep tests are spot welded on the rear face of the specimens. During creep tests, specimen surface was captured through a slot machined in the radiant furnace with a high-resolution CCD camera (AVT Manta G-917B) with a resolution of 9 million pixels and 10 Hz acquisition frequency. Strain marker detection used in-house software. The data were post-processed to obtain the strain evolution along the loading direction at the surface of each grain. EBSD measurements were performed after tests to obtain average lattice rotation per grain induced during creep.

2.5. Creep tests with Digital Image Correlation

Creep tests were performed using a INSTRON 5582 universal testing machine equipped with EASYHEAT induction heating system. An in-house induction coil (Figure 4(a) and Figure 15(a)) was used to minimize the temperature gradient across the creep specimen. In addition, it gives visual access to the entire surface of the specimen. The coil induces a temperature gradient of about 15°C (at 740°C) across the specimen gauge length. A two colors pyrometer provides temperature measurements at the surface of the specimen. A closed-loop system was used between the pyrometer and induction heating system to adjust the induction power to maintain a constant temperature during creep tests. The coil was maintained by high-temperature resistant fiberglass material to position the coil in relation to the specimen carefully. The rig comprises a Nikon D5300 digital camera with a CCD resolution of 6036×4020 pixels. AF-S DX Nikkor 18-55 mm f1:3.5 macro lens was used. The magnification factor corresponds to a resolution of 80 pixels/mm, i.e., one pixel corresponds to 12.5 μm. A polarized lens filter is used to capture the surface of the specimen during creep tests at high temperatures. A ORIENTAL MOTOR high resolution hollow rotary actuator allowed rotation of the camera around the gauge length of the specimen. High-resolution images before and during creep tests were processed for each rotation step by digital image correlation using the commercial Vic-2D 2009 software. Before imaging, a sprayed speckle pattern suitable for strain measurement was applied at the surface of the specimen using an airbrush kit and high-temperature resistant paint ((Figure 4(c)). Circular particles with a diameter in the order of 50 microns were obtained. Strain fields were obtained at the surface of the specimen during creep test by digital image correlation using a subset and step size of 21×21 pixels and 5 pixels, respectively. A decay filter of 5×5 was used to calculate the strain field. Such procedure allowed in-plane strain field measurements along the loading direction for the entire gauge length by doing a 360° rotation of the rig. A rotation step of 15° was used during the creep test.

3. Results

The creep behavior of the GTD444 specimens was reported elsewhere [11] and will be discussed later in this article. Results for the DS200 alloy are reported in the present section. Creep behavior of DS200 specimens extracted along the longitudinal and transverse direction and tested at 750°C and 800 MPa are presented in Figure 5 and compared to the creep behavior of a single crystal (SX) Mar-M200 specimen. Detail of the primary creep regime is provided in Figure 5(b). Creep behavior for specimens tested at 900°C and 350 MPa are presented in Figure 6(a-c) for a single crystal (SX) Mar-M200 specimen and for DS200 specimens extracted along the longitudinal and transverse directions. Creep life for specimens tested at 900°C is shown in Figure 6(d) as a function of the apply stress in the range of 250 MPa to 400 MPa.

For both investigated creep conditions, single crystal Mar-M200 and DS200 specimens extracted along the longitudinal direction display similar creep behavior with the presence of the primary, secondary and tertiary creep regimes. A decrease in creep lifetime is reported for the DS200 specimens extracted along the longitudinal direction in comparison to the single crystal Mar-M200 specimen. It is classically associated with the average orientation of the DS200 specimens extracted along the longitudinal direction being misoriented to the optimum <001> orientation [13, 25, 14]. In contrast, a tertiary creep regime at 900°C and 350 MPa and secondary creep regime at 750°C and 800 MPa is not observed for DS200 specimens extracted along the transverse direction. Consequently, creep lifetime is the lowest for DS200 specimens extracted along the transverse direction. Interestingly, the creep strain rate evolution in the primary and secondary creep regimes are similar for single crystal Mar-M200 and DS200 specimens extracted along longitudinal and transverse directions as shown in Figure 6(c), indicating similar intrinsic creep behavior. However, early fractures are reported for the DS specimens extracted along the transverses direction. The fracture surface of a DS200 specimen extracted along the transverse direction is presented in Figure 7 for creep test conditions of 900°C and 350 MPa. The roughness of the fracture surface correlates with the profile of the serrated grain boundaries observed in Figure 2(a) indicating intergranular fracture. Unlike the single crystals Mar-M200 specimens (not presented), the fracture surface of all failed DS creep specimens extracted along the transverse direction remained quasi-circular. In addition, it is also observed the presence of a high density of carbides along the fracture surface of DS200 specimens as shown in Figure 7(b).

3.1. Creep mechanisms for DS specimens extracted along the transverse direction

Creep tests with strain markers (see section 2.4) were performed on DS200 specimens extracted along the transverse direction at 750°C and 700 MPa, 750°C and 750 MPa, 750°C and 800 MPa and 900°C and 400 MPa. The microstructures along the gauge sections of the investigated specimens are reported in Figure 8. White arrows in Figure 8 indicate the location of crack nucleation during creep tests. It is systematically observed that crack nucleation occurs at transverse grain boundaries. This observation is in agreement with intergranular initiation observed on the fracture surface as shown in Figure 7. Evolution of the strain along the loading direction is extracted for grains labeled "G1" to "G18" during creep tests using strain marker measurements (see section 2.4) and displayed in Figure 9. As reported from the creep curves in Figure 5, specimen fracture occurs after a few hours for specimens tested at 750°C and 700 MPa, 750°C and 750 MPa, and 750°C and 800 MPa. Interestingly, significant creep strain variations are observed from one grain to another. High differences in creep strain are reported for grains that display orientation along the loading direction close to <001> (red grains in Figure 8) and <101> (green grains in Figure 8). Moreover, differences in creep strain from grain to grain are reported to a limited extent for specimens tested at 900°C and 400 MPa, Figure 9(d).

Primary (fatal) and secondary crack nucleation sites are grain boundaries described by two crystallographic orientations along the loading direction of the grains they delimit. These orientations are reported for the investigated specimens after rupture in Figure 10(a and b) respectively for all examined conditions. The lines in Figure 10 connect the orientation of the grains on one side to the other of an initiated grain boundary. Interestingly, the grain boundaries where crack nucleated display a high level of misorientation (up to 40°) along the loading direction, indicating that high angle grain boundaries (HAGBs) are the preferential sites for crack nucleation. In addition, grain boundaries that delimit grains with orientation along the loading direction close to <001> and <101> are preferential nucleation sites for a low temperature

condition (750°C). For specimens tested at 900°C, the misorientation between the grains that display primary and secondary crack nucleation is observed to be somewhat lower in comparison to the misorientation observed for specimens tested at 750°C. In addition, a higher number of secondary cracks are observed for the specimen tested at 900°C in comparison to specimens tested at a low temperature. Strain evolution measured by DIC is shown in Figure 11 (see section 2.5) for a DS200 along the transverse direction after testing at 740°C and 700 MPa as the function of the creep life. Two profiles along the gauge length of the same specimen along the loading direction are displayed in Figure 11(a and b) respectively. Red and black arrows locate the primary and a secondary crack, respectively. The fluctuation in strain along the gauge length is in the order of 1% early in creep and this is correlated with strain fluctuations from one grain to another as observed in Figure 9 from strain marker tests. In addition, the strain at the location where cracks nucleated increases significantly near the end of the creep life due to the presence of the crack. Therefore, crack nucleation is observed to occur near the end of the creep life and crack propagation along the grain boundaries is rapid. The orientation of the grain boundaries that are primary and secondary nucleation sites are reported in Figure 12 and are similar to the ones observed using strain marker tests.

The evolution of the average crystallographic orientation during creep tests at 750°C, 700 and 750 MPa for grains of interest labeled "G1" to "G8" in Figure 8 are presented in Figure 13. Significant lattice rotations of up to 6° toward the direction of the <001> pole was observed for grains "G1" and "G3", toward the <111> direction for grains "G4", "G6" and "G8" and the direction of the line <001>- <111> for grains "G2", "G5" and "G7".

The precipitate structure after creep tests at 750°C and 750 MPa is reported in Figure 14(a and b). Almost no $\gamma\prime$ morphology evolution is observed after creep at this condition. In addition, evidence of a high degree of localized shearing of the $\gamma\prime$ precipitates (Figure 14(b)) is observed across the entire gauge length. The evolution of the precipitate structure during the creep test at 900°C and 400 MPa is shown in Figure 14(c and d) using interrupted creep after 24.8 and 41.8 hours. The $\gamma\prime$ rafting phenomenon is clearly observed. However, no evidence of $\gamma\prime$ shearing is observed.

Strain measurements were also performed during creep testing at 750°C and 700 MPa on a GTD444 specimen that displayed a unique transverse grain boundary (see Figure 2(d)). The evolution of the average strain along the loading direction on both sides of the grain boundary is displayed in Figure 15(b). The strain maps and strain profiles along the gauge length are reported in Figure 15(c and b) during creep life. The grain labeled "side 1" displays a large evolution of strain during the creep test, while the other labeled "side 2" shows a relatively low strain accumulation during creep. Near the end of the creep life, a significant rise in strain is observed at the grain boundary, evidencing crack nucleation and rapid crack propagation. The fracture surface of the specimen in Figure 16 displays intergranular crack nucleation. It is interesting to note a few crystallographic facets (black arrow, for instance) across the fracture surface in Figure 16(b).

4. Discussion

While the creep strain rate is similar in the single crystal Mar-M200 and DS200 specimens, the creep life and creep strain at rupture are significantly diminished for the DS200 specimens extracted along the transverse direction. The decrease in creep life and creep strain at rupture is even more pronounced for specimens tested in a low temperature and high-stress condition (750°C and 800 MPa). The rupture of the DS200 specimens extracted along the transverse loading direction is observed to occur at the end of the primary regime for specimens tested at high stress and low temperature (750°C and 800 MPa) while occurring during the secondary regime for specimens tested at high temperature (900°C) and low stresses (900°C and 250 MPa to 400 MPa). The substantial decrease observed in creep life and creep strain at rupture have previously been reported for different Ni-based superalloys during transverse creep and explained by the development of significant stress concentration near HAGBs [11, 13] or/and by oxidation assisted crack nucleation [13, 14]. Similar results were also observed recently by Torfeh et al. [27] for GTD111DS tested along longitudinal direction or by Alkmin et al. [28] in conventional cast Mar-M246. Stinville et al. [11] observed on GDT444 bycrystals with transverse grain boundaries rupture before the tertiary creep regime. They demonstrated that the evolution of the lattice rotation and associated differential shape changes on both sides of a transverse grain boundary enhanced local plasticity in the vicinity of the

HAGBs, resulting in early crack nucleation. In the present study, for DS200 specimens extracted along the transverse direction, the rupture similarly occurs before the tertiary creep regime, diminishing the creep strain at rupture. Orientation evolution during creep is also observed in Figure 13, as previously reported [11, 13, 19]. In addition, different strain evolution is observed from grain to grain in the present study, as observed in Figure 9. Both differential strain evolution from grain to grain and lattice rotation enhance strain/stress incompatibilities, favoring crack nucleation at transverse grain boundaries. The present study also uncovers the grain boundary configurations that promote crack nucleation. DS200 specimens extracted along the transverse direction and tested at a low temperature (740°C - 750°C) and high stress display crack nucleation at grain boundary that maximizes misorientation along the loading direction across the boundary as shown in Figure 10 and Figure 12. Large misorientation across grain boundaries favors stress incompatibilities during deformation, especially at grain boundaries separating a grain which has limited rotation (e.g. <001> oriented) and a grain favorably oriented for single slip activity [29]. Interestingly HAGBs that display one of their grains with an orientation in the "middle" of the inverse pole figure are also preferred sites for crack nucleation. While these boundaries do not maximize grain boundary misorientation, the grains with orientation along the loading direction close to the "middle" of the inverse pole figure have specificity. These grains display a high Schmid factor, i.e., high resolved shear stresses. As observed in Figure 14(b) for a low temperature and high-stress condition, shearing events are present and are known to favor the accumulation of single slip and lattice rotation [30]. Crystallographic facets are observed on the fracture surfaces of specimens tested under a low temperature creep condition, as evidenced in Figure 16(b). Intense precipitate shearing events play an important role in damage nucleation from grain boundaries and carbides located in their vicinity. Shearing is facilitated for grains that display high resolved shear stress, i.e., orientation along the loading direction in the middle of the inverse pole figure. Moreover, the grains with orientation in the middle of the inverse pole figure have the specificity to not reorient extensively under deformation accommodating to a less extent the deformation [30, 31].

For tests conditions at a low temperature (750°C) and high stress, two grain boundary configurations are preferential crack nucleation sites. However, for tests conditions at high temperature (900°C) and low stress, multiple boundary configurations are observed to be preferred site for crack nucleation, Figure 10. Under high temperature and low stress conditions the difference in creep strain evolution observed from grain to grain are lower, Figure 9. In addition, no obvious long-range precipitate shearing were observed for specimen tested at the high temperature and low-stress condition. At such a high temperature, deformation is occurring more isotropically by the activation of multiple slip systems, homogenizing the localization of the plasticity [32, 33, 34]. With $\gamma\prime$ rafting progressing, easier plastic flow by glide and climb in the γ matrix around the precipitates is activated, leading overall to more active slip systems and a more homogeneous deformation [32, 33, 34]. It is therefore expected a lower level of grain rotation on both sides of the boundaries. Consequently, a lower level of stress incompatibility is expected at the HAGBs, providing competitive crack nucleation sites. In addition, oxidation assisted crack nucleation may play an important role at 900°C. Oxidation assisted crack nucleation of DS200 does not seem to be highly sensitive to grain boundary misorientation [14].

For creep at a low temperature (750°C) and high stress, it is observed higher stress incompatibly at HAGBs evidenced by shearing events, differential creep strain from grain to grain and lattice rotation in comparison to specimen tested at high temperature (900°C) and low stress. Consequently, specimen fracture occurs in a earlier regime (during primary creep regime) at a low temperature than at high temperature (during secondary). Moreover, the high stress incompatibility promote rapid crack propagation as evidenced by the rapid rise in strain at the HAGBs during in-situ testing on the GTD444 (Figure 15) and DS200 (Figure 11) specimens.

5. Conclusions

Directionally solidified Ni-based superalloy DS200 and GTD444 have been investigated under transverse creep at an intermediate (750°C) and high stress, and high temperatures (900°C) and low stress for DS200 only. The following conclusion can be established from this work:

- Intergranular crack nucleation (and subsequent propagation) along transverse high angle grain boundaries is observed at an intermediate and high temperatures, decreasing creep lifetime and creep strain at rupture in comparison to single crystal or longitudinal creep.
- Two type of columnar grain configurations are observed to promote damage at an intermediate temperature and high stress. With increasing test temperature, no specific grain boundaries configuration is observed to trigger cracking, due to a greater contribution of grain boundary oxidation.
- High strain/stress incompatibilities at high angle grain boundaries during transverse creep at an intermediate temperature lead to crack nucleation in the primary creep regime. Strain/stress incompatibilities at high angle grain boundaries during transverse creep at high temperature is observed to a limited extent inducing crack nucleation in the secondary creep regime. These incompatibilities are observed as a result of single slip activity at the grain scale, leading to local crystallographic rotation.

6. Acknowledgments

Safran (Safran SA and Safran Aircraft Engines) is gratefully acknowledged for providing DS200 plates and Mar-M200 SX bars, for financial support and for L.M.S. doctoral grant. Pr. Georges Cailletaud (Mines ParisTech), Dr. Florent Coudon (SAFRAN Tech) and Dr. Denis Bertheau (Institut Pprime) are acknowledged for the scientific discussions and their relevant suggestions. TMP is grateful for the support of a Vannevar Bush DoD Faculty Fellowship, ONR Grant N00014-18-1-3031. J.C.S. is grateful for financial support from startup funds provided by the Department of Materials Science and Engineering at University of Illinois at Urbana-Champaign and from the Energy & Biosciences Institute (EBI) through the EBI-Shell Program.

7. Data availability

Data will be made available on request.

References

[1] M. Donachie, S. Donachie, Superalloys: A Technical Guide, 2nd Edition, Ingenieria de minas, ASM International, 2002.

[2] R. C. Reed, The Superalloys, Cambridge University Press, 2006, cambridge Books Online.

[3] M. Gell, D. Duhl, A. Giamei, The development of single crystal superalloy turbine blades, in: Superalloys 1980 (Fourth International Symposium), TMS, 1980. doi:10.7449/1980/superalloys$_1$980$_2$05$_2$14.

[4] F. Coudon, G. Cailletaud, J. Cormier, L. Marcin, A multiscale model for nickel-based directionally solidified materials, International Journal of Plasticity 115 (2019) 1–17. doi:https://doi.org/10.1016/j.ijplas.2018.10.003.

[5] J. Li, N. Tian, P. Zhang, F. Yu, G. Zhao, P. Zhang, Creep damage and deformation mechanism of a directionally solidified alloy during moderate-temperature creep, Crystals 11 (6). doi:10.3390/cryst11060646.

[6] J. J. Jackson, M. J. Donachie, M. Gell, R. J. Henricks, The effect of volume percent of fine γ' on creep in ds mar-m200 + hf, Metallurgical Transactions A 8 (10) (1977) 1615–1620. doi:10.1007/BF02644867.

[7] W. An, S. Utada, X. Guo, S. Antonov, W. Zheng, J. Cormier, Q. Feng, Thermal cycling creep properties of a directionally solidified superalloy dz125, Journal of Materials Science Technology 104 (2022) 269–284. doi:https://doi.org/10.1016/j.jmst.2021.07.015.

[8] M. Kirka, K. Brindley, R. Neu, S. Antolovich, S. Shinde, P. Gravett, Parameters influencing thermomechanical fatigue of a directionally-solidified ni-base superalloy, International Journal of Fatigue 81 (2015) 48–60. doi:https://doi.org/10.1016/j.ijfatigue.2015.07.011.

[9] D. Shi, J. Liu, X. Yang, H. Qi, J. Wang, Experimental investigation on low cycle fatigue and creepâĂŞfatigue interaction of dz125 in different dwell time at elevated temperatures, Materials Science and Engineering: A 528 (1) (2010) 233–238, special Topic Section: Local and Near Surface Structure from Diffraction. doi:https://doi.org/10.1016/j.msea.2010.08.089.

[10] X.-A. Hu, X.-G. Yang, D.-Q. Shi, H.-C. Yu, T.-T. Ren, Constitutive modeling of a directionally solidified nickel-based superalloy dz125 subjected to thermal mechanical creep fatigue loadings, Rare Metals 38 (10) (2019) 922–936. doi:10.1007/s12598-016-0713-8.

[11] J. C. Stinville, K. Gallup, T. M. Pollock, Transverse Creep of Nickel-Base Superalloy Bicrystals, Metallurgical and Materials Transactions A 46 (6) (2015) 2516–2529. doi:10.1007/s11661-015-2869-5.

[12] B. DeMestral, G. Eggeler, H. J. Klam, On the influence of grain morphology on creep deformation and damage mechanisms in directionally solidified and oxide dispersion strengthened superalloys, Metallurgical and Materials Transactions A 27 (4) (1996) 879–890. doi:10.1007/bf02649755.

[13] L. M. Suave, J. Cormier, P. Villechaise, D. Bertheau, G. Benoit, G. Cailletaud, L. Marcin, Anisotropy in creep properties of ds200 + hf alloy, Materials at High Temperatures 33 (4-5) (2016) 361–371. arXiv:https://doi.org/10.1080/09603409.2016.1159836, doi:10.1080/09603409.2016.1159836.

[14] L. Mataveli Suave, A. S. Muñoz, A. Gaubert, G. Benoit, L. Marcin, P. Kontis, P. Villechaise, J. Cormier, Thin-wall debit in creep of ds200 + hf alloy, Metallurgical and Materials Transactions A 49 (9) (2018) 4012–4028. doi:10.1007/s11661-018-4708-y.

[15] D. Shi, C. Dong, X. Yang, Constitutive modeling and failure mechanisms of anisotropic tensile and creep behaviors of nickel-base directionally solidified superalloy, Materials Design 45 (2013) 663–673. doi:https://doi.org/10.1016/j.matdes.2012.09.031.

[16] J. Huang, D. Shi, X. Yang, A modern and robust methodology for modeling anisotropic creep characteristics of ni-based ds and sc superalloys, Science China Technological Sciences 57 (9) (2014) 1802–1815. doi:10.1007/s11431-014-5610-5.

[17] B. Yan, J. Zhang, L. Lou, Effect of boron additions on the microstructure and transverse properties of a directionally solidified superalloy, Materials Science and Engineering: A 474 (1) (2008) 39–47. doi:https://doi.org/10.1016/j.msea.2007.05.082.

[18] M. Shenoy, D. McDowell, R. Neu, Transversely isotropic viscoplasticity model for a directionally solidified ni-base superalloy, International Journal of Plasticity 22 (12) (2006) 2301–2326. doi:https://doi.org/10.1016/j.ijplas.2006.03.003.

[19] D. Kobayashi, M. Miyabe, M. Achiwa, R. Sugiura, A. T. Yokobori, CreepâĂŞfatigue crack growth behaviour based on ebsd observations for notched specimen made of directionally solidified ni-base superalloy, Materials at High Temperatures 31 (4) (2014) 326–333. arXiv:https://doi.org/10.1179/0960340914Z.00000000043, doi:10.1179/0960340914Z.00000000043.

[20] D. N. Duhl, C. P. Sullivan, Some effects of hafnium additions on the mechanical properties of a columnar-grained nickel-base superalloy, JOM 23 (7) (1971) 38–40. doi:10.1007/BF03355714.

[21] Q. Chen, C. Jones, D. Knowles, The grain boundary microstructures of the base and modified rr 2072 bicrystal superalloys and their effects on the creep properties, Materials Science and Engineering: A 385 (1) (2004) 402–418. doi:https://doi.org/10.1016/j.msea.2004.07.013.

[22] J. C. Stinville, W. C. Lenthe, J. Miao, T. M. Pollock, A combined grain scale elastic-plastic criterion for identification of fatigue crack initiation sites in a twin containing polycrystalline nickel-base superalloy, Acta Materialia 103 (2015) 461–473. doi:10.1016/j.actamat.2015.09.050.

[23] Q. Chen, N. Jones, D. Knowles, The microstructures of base/modified rr2072 sx superalloys and their effects on creep properties at elevated temperatures, Acta Materialia 50 (5) (2002) 1095–1112. doi:https://doi.org/10.1016/S1359-6454(01)00410-4.

[24] A. J. Elliott, T. M. Pollock, S. Tin, W. T. King, S.-C. Huang, M. F. X. Gigliotti, Directional solidification of large superalloy castings with radiation and liquid-metal cooling: A comparative assessment, Metallurgical and Materials Transactions A 35 (10) (2004) 3221–3231. doi:10.1007/s11661-004-0066-z.

[25] L. M. Suave, J. Cormier, P. Villechaise, D. Bertheau, F. Mauget, G. Cailletaud, L. Marcin, High temperature creep damage mechanisms in a directionally solidified alloy: impact of crystallography and environment, Superalloy 2016,M. Hardy, E. Huron, U. Glatzel, B. Griffin, B. Lewis, C. Rae, V. Seetharaman, S. Tin (Eds.), Superalloys 2016, TMS, Seven Springs, Champion, PA, USA (2016) (2016) 747 – 756.

[26] J. Cormier, M. Jouiad, F. Hamon, P. Villechaise, X. Milhet, Very high temperature creep behavior of a single crystal ni-based superalloy under complex thermal cycling conditions, Philosophical Magazine Letters 90 (8) (2010) 611–620. arXiv:https://doi.org/10.1080/09500839.2010.489887, doi:10.1080/09500839.2010.489887.

[27] M. Torfeh, S. M. H. Mirbagheri, J. Cormier, J. A. Mohandesi, S. Nakhodchi, Intermediate temperature creep damage mechanisms of a directionally solidified ni-based superalloy, Materials at High Temperatures 0 (0) (2022) 1–13.

arXiv:https://doi.org/10.1080/09603409.2022.2046386, doi:10.1080/09603409.2022.2046386.

[28] L. Alkmin, S. Utada, N. Chaia, D. Reis, G. Coelho, J. Cormier, C. Nunes, Creep behavior of conventional and nb-modified as-cast mar-m246 superalloy, Materials Science and Engineering: A 813 (2021) 141170. doi:https://doi.org/10.1016/j.msea.2021.141170.

[29] R. A. MacKay, R. D. Maier, The influence of orientation on the stress rupture properties of nickel-base superalloy single crystals, Metallurgical Transactions A 13 (10) (1982) 1747–1754. doi:10.1007/BF02647830.

[30] C. Rae, R. Reed, Primary creep in single crystal superalloys: Origins, mechanisms and effects, Acta Materialia 55 (3) (2007) 1067–1081. doi:https://doi.org/10.1016/j.actamat.2006.09.026.

[31] G. I. Taylor, Plastic strain in metals, Journal of the Institute of Metals 62 (1938) 307 – 324.

[32] A. Epishin, T. Link, U. BrÃijckner, P. Portella, Kinetics of the topological inversion of the Î§/Î§âĂš-microstructure during creep of a nickel-based superalloy, Acta Materialia 49 (19) (2001) 4017–4023. doi:https://doi.org/10.1016/S1359-6454(01)00290-7.

[33] A. Epishin, T. Link, H. KlingelhÃűffer, B. Fedelich, P. Portella, Creep damage of single-crystal nickel base superalloys: mechanisms and effect on low cycle fatigue, Materials at High Temperatures 27 (1) (2010) 53–59. arXiv:https://doi.org/10.3184/096034009X12603595726283, doi:10.3184/096034009X12603595726283.

[34] R. Reed, N. Matan, D. Cox, M. Rist, C. Rae, Creep of cmsx-4 superalloy single crystals: effects of rafting at high temperature, Acta Materialia 47 (12) (1999) 3367–3381. doi:https://doi.org/10.1016/S1359-6454(99)00217-7.

[35] G. Bouse, M. Henry, J. Schaeffer, Nickel base superalloys and turbine components fabricated therefrom, US Patent 5,154,884.

Table 1: Composition, in weight percent, of the Ni-based superpalloys Mar-M200, DS200 and GTD444 investigated in this study. The DS200 is the directionally solidify version of the single crystal Mar-M200. DS200 and Mar-M200 display significant amount of Hafnium.

	Cr	Co	Mo	W	Ta	Nb	Al	Ti	Hf	Re	C	B	Ni	Ref.
Mar-M200	8.6	9.5	-	11.8	-	0.86	4.90	1.87	1.58	-	0.13	0.015	Bal.	
DS200	8.6	9.5	-	11.8	-	0.86	4.90	1.87	1.58	-	0.13	0.015	Bal.	
GTD444	9.7	8	1.5	6	4.7	0.5	4.2	3.5	0.15	-	0.09	0.009	Bal.	[35]

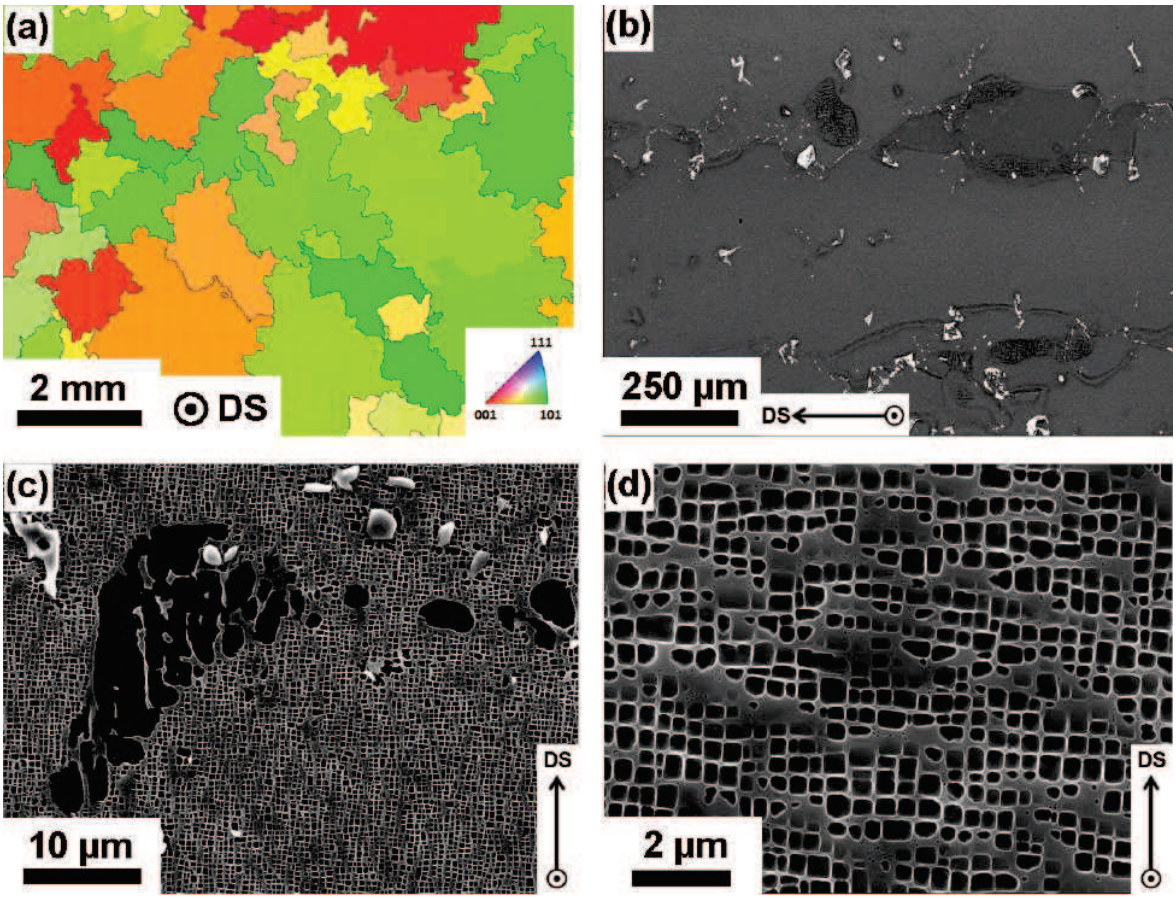

Figure 1: Microstructure of a DS200 specimen in a plane perpendicular to the solidification direction: (a) at the grain scale characterized by EBSD; (b) at the dendritic scale characterized by secondary electron images; (c) at the location of a γ-γ' eutectic pools; (d) in a primary dendrite arm.

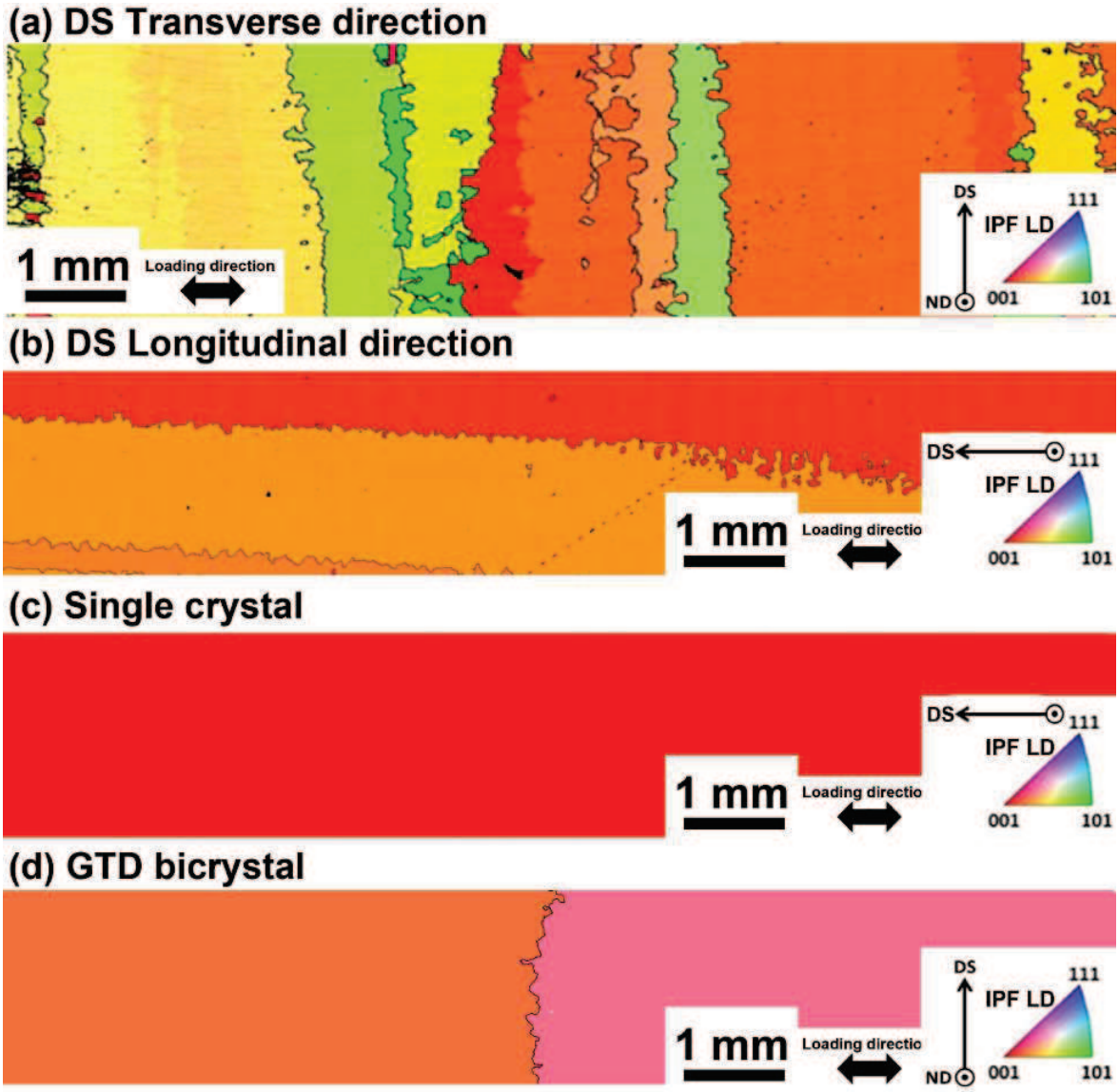

Figure 2: Microstructural configuration of the investigated creep specimens from EBSD measurements: (a) Ni-based superalloy DS200 specimen with gauge length along the transverse direction; (b) Ni-based superalloy DS200 specimen with gauge length along the longitudinal direction; (c) Mar-M200 single crystal; (d) Ni-based superalloy GTD444 bicrystal specimen.

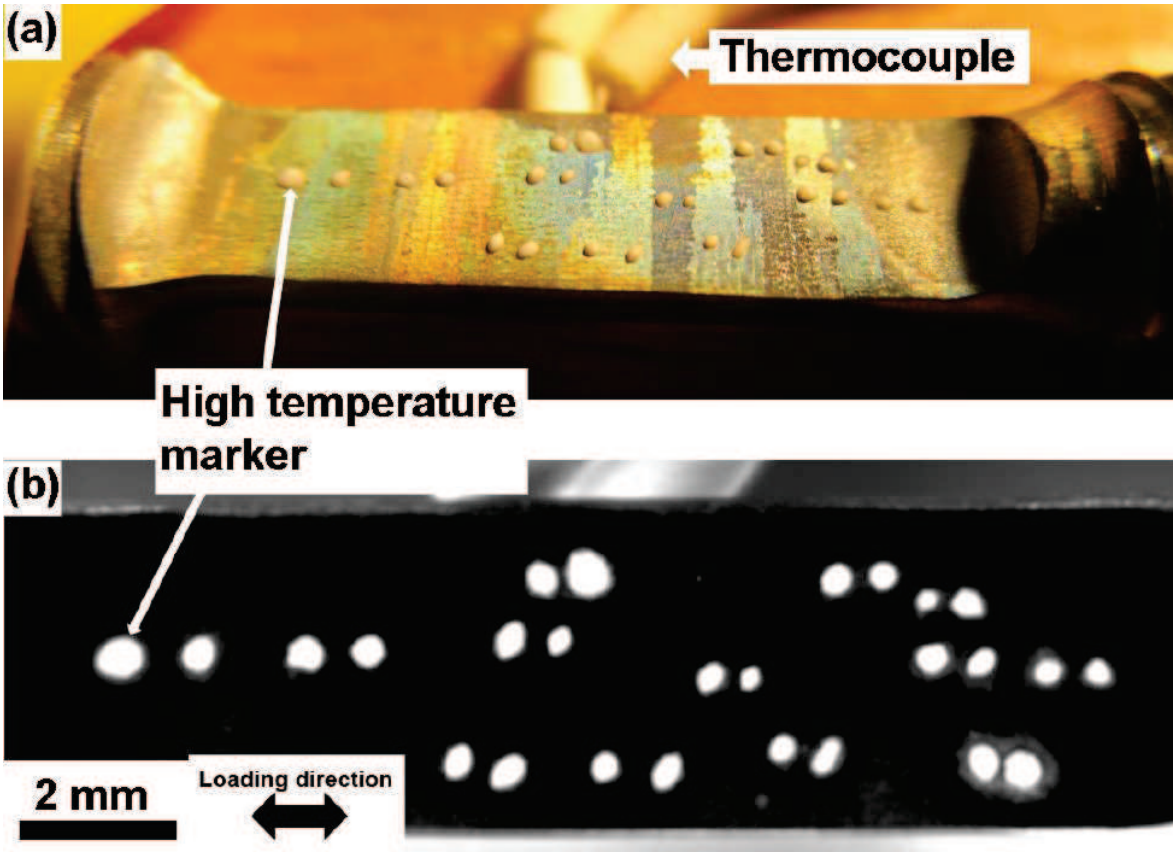

Figure 3: (a) A DS200 specimen extracted along the transverse direction equipped with strain markers prior to creep test. Grains of interest display two strain markers across their length to capture their deformation during creep life. (b) In-situ observation of the strain markers during high temperature creep test.

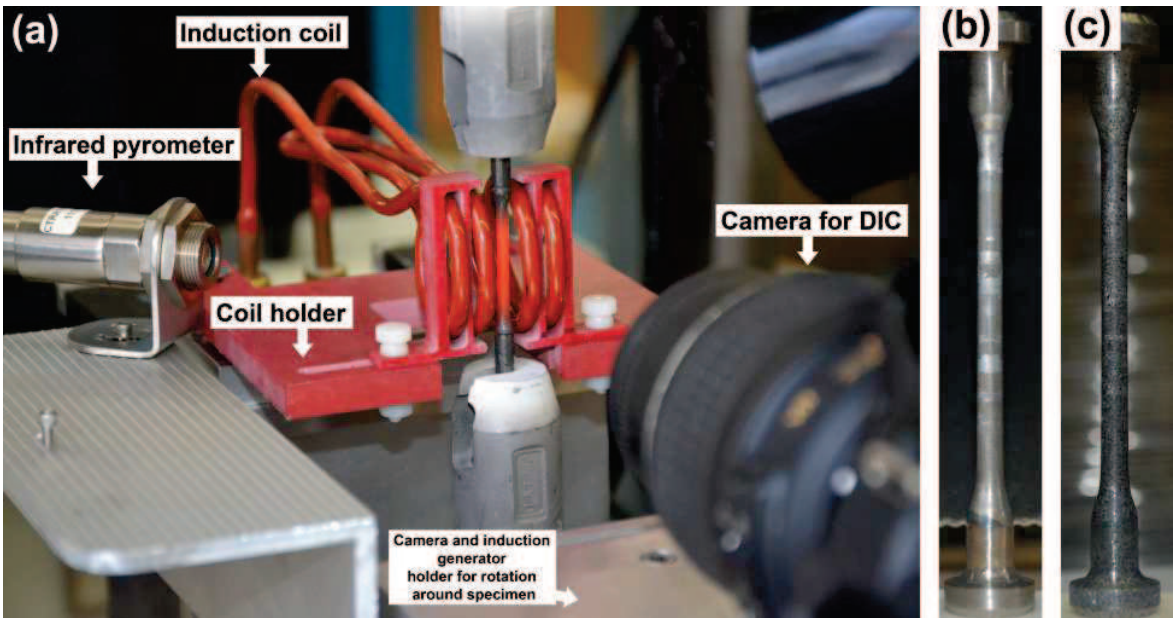

Figure 4: (a) Experimental setup for high temperature creep with strain measurements by optical digital image correlation. The infrared pyrometer provides the temperature of the specimen and is in a closed loop system with the induction heating system to adjust the induction power to maintain constant temperature during creep test. The camera, pyrometer and induction system is rotating around the specimen to capture images across the entire surface of the specimen while maintaining constant temperature and load during creep test. A DS200 specimen before (b) and after (c) high temperature pattern deposition for digital image correlation measurements.

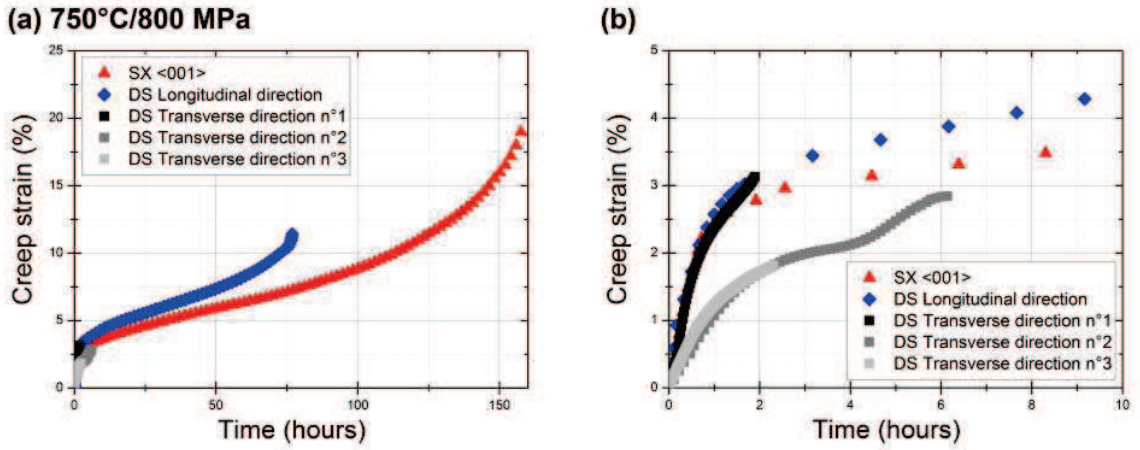

Figure 5: (a) Creep behavior (up to failure) at 750°C and 800 MPa of a <001>-single crystal Mar-M200 specimen and DS200 specimens extracted along both longitudinal and transverse loading directions. (b) A magnification on the first 10 hours of creep testing to show the variability in creep behavior for DS200 specimens tested along transverse direction.

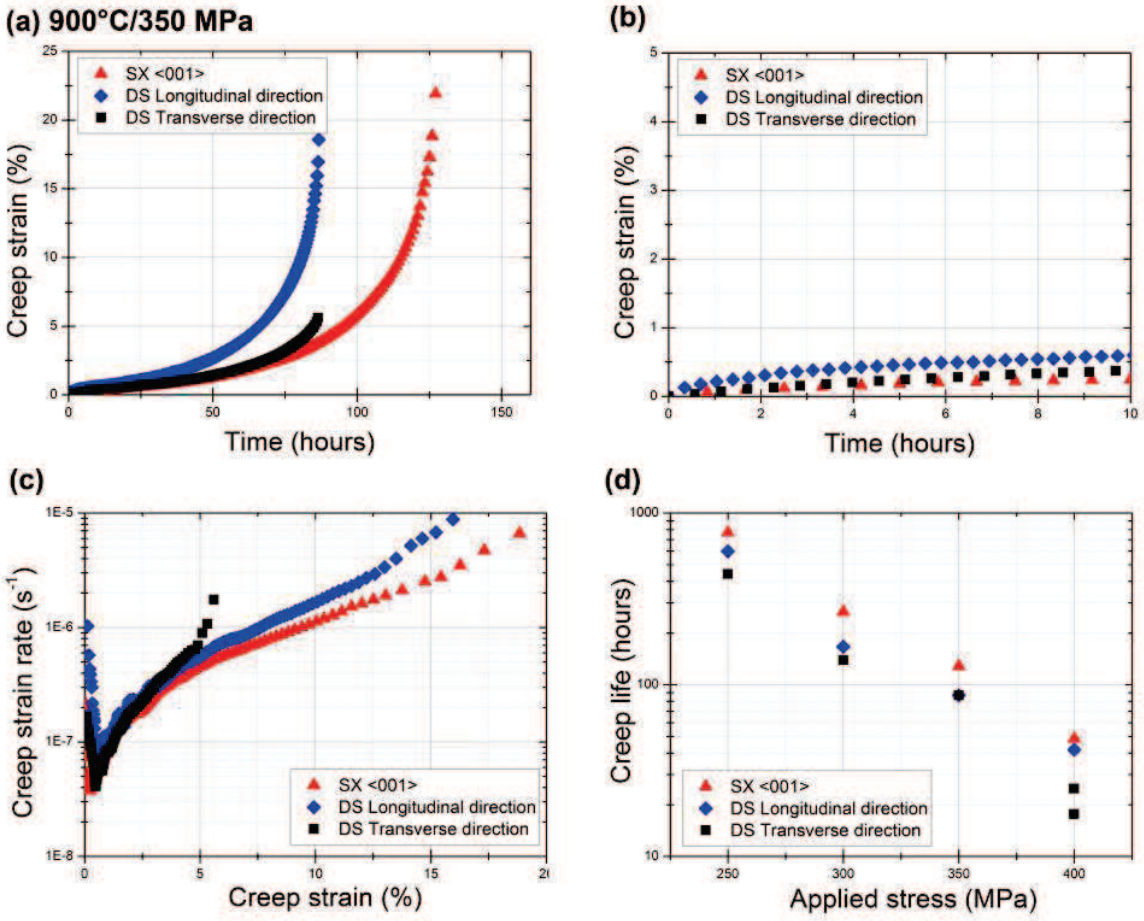

Figure 6: (a) Creep behavior (up to failure) at 900°C and 350 MPa of a <001>-single crystal Mar-M200 specimen and DS200 specimens extracted along both longitudinal and transverse loading directions. (b) A magnification on the first 10 hours of creep testing. (c) Creep strain rate versus creep strain for the investigated specimens. (d) Creep life evolution at 900°C as a function of the applied stress.

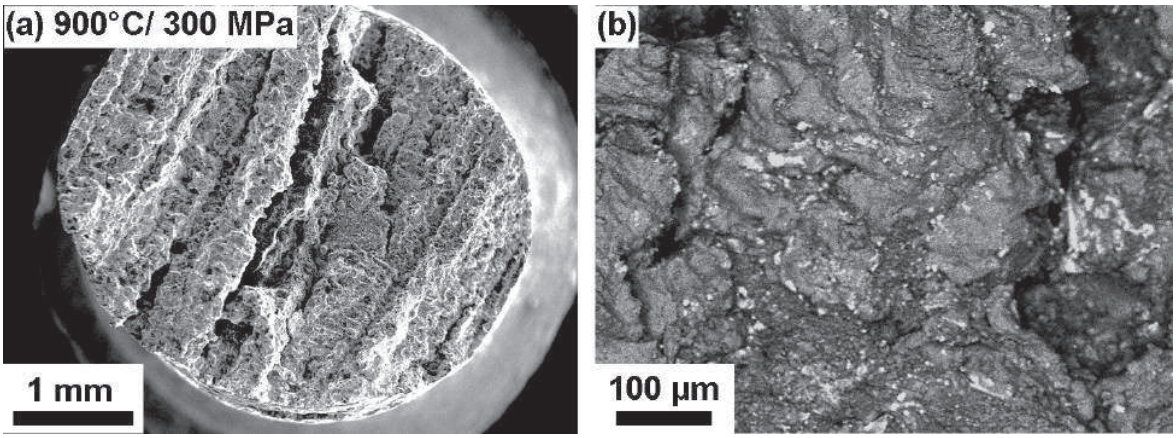

Figure 7: Fracture surface of a DS200 specimen extracted along the transverse direction after creep testing at 900°C and 300 MPa. Intergranular fracture mode (a) and carbides networks associated with grain boundaries (b) are observed.

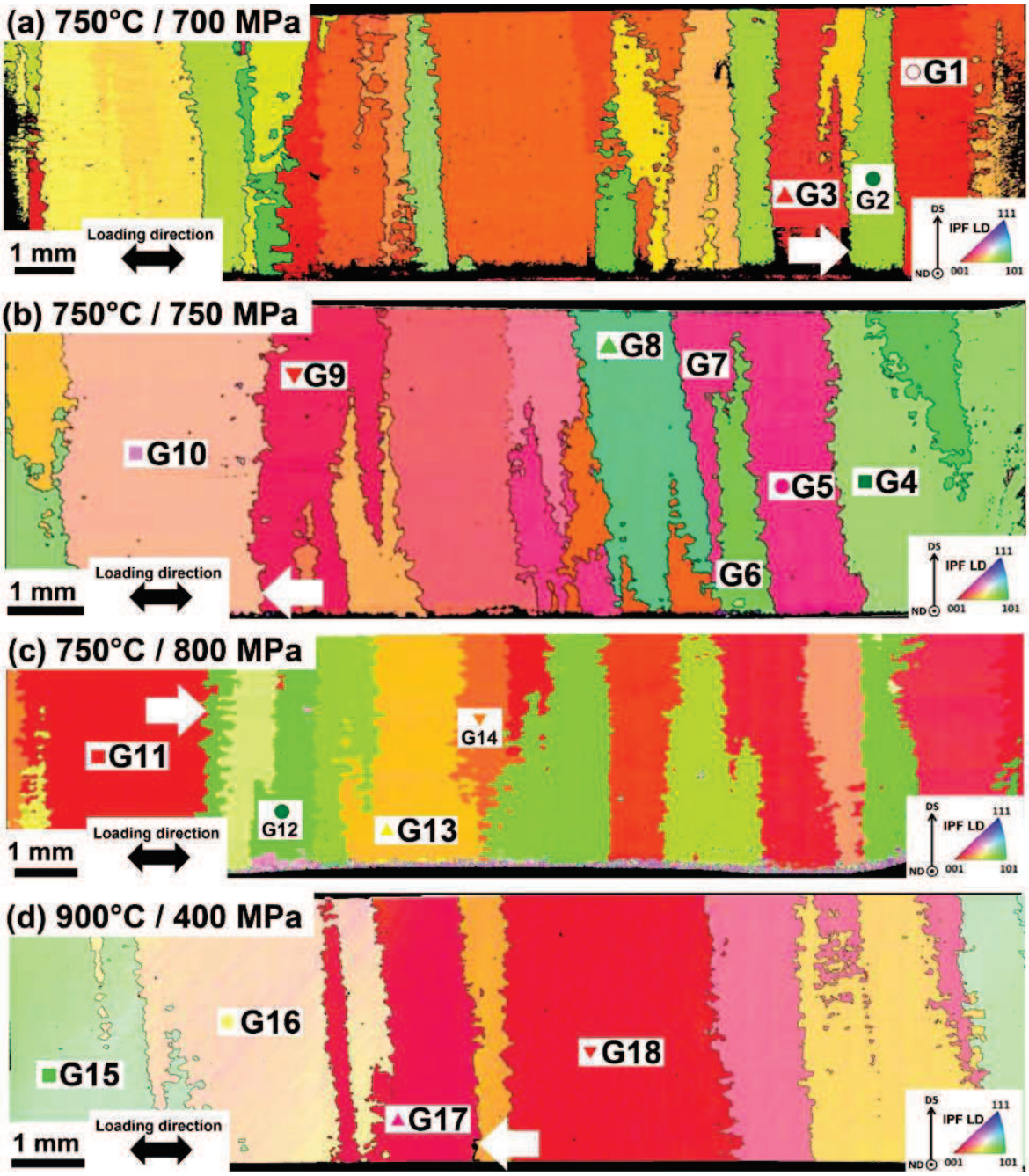

Figure 8: EBSD characterizations before creep deformation of DS200 specimens extracted along the transverse direction. Creep tests are performed with strain markers at 750°C and 700 MPa (a), 750°C and 750 MPa (b), 750°C and 800 MPa (c) and 900°C and 400 MPa (d). White arrows highlight location of intergranular crack initiation. Grains of interest where strain is extracted by strain markers measurements are labeled "G1" to "G18".

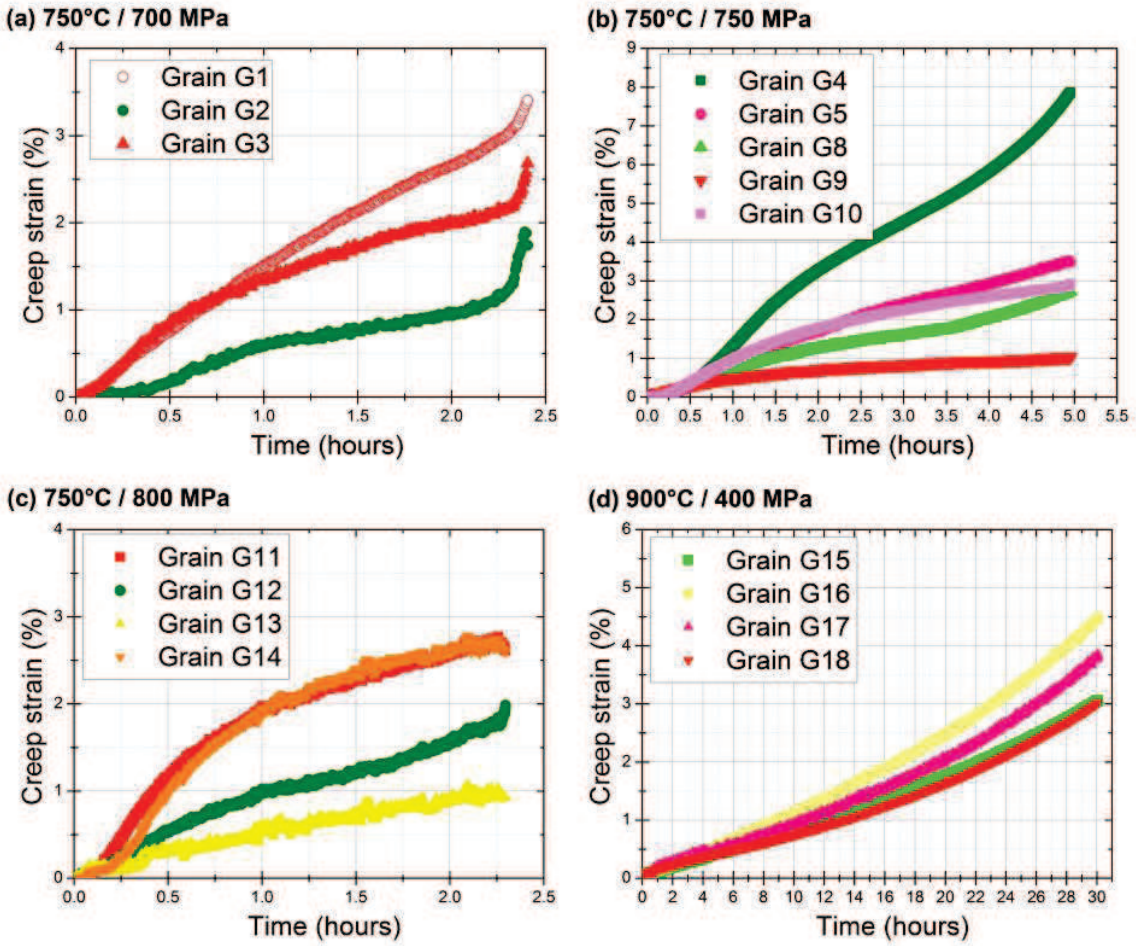

Figure 9: Creep strain (along loading direction) evaluation by strain marker measurements in grains labeled "G1" to "G18" as identified in Figure 8 at 750°C and 700 MPa (a), 750°C and 750 MPa (b), 750°C and 800 MPa (c) and 900°C and 400 MPa (d)

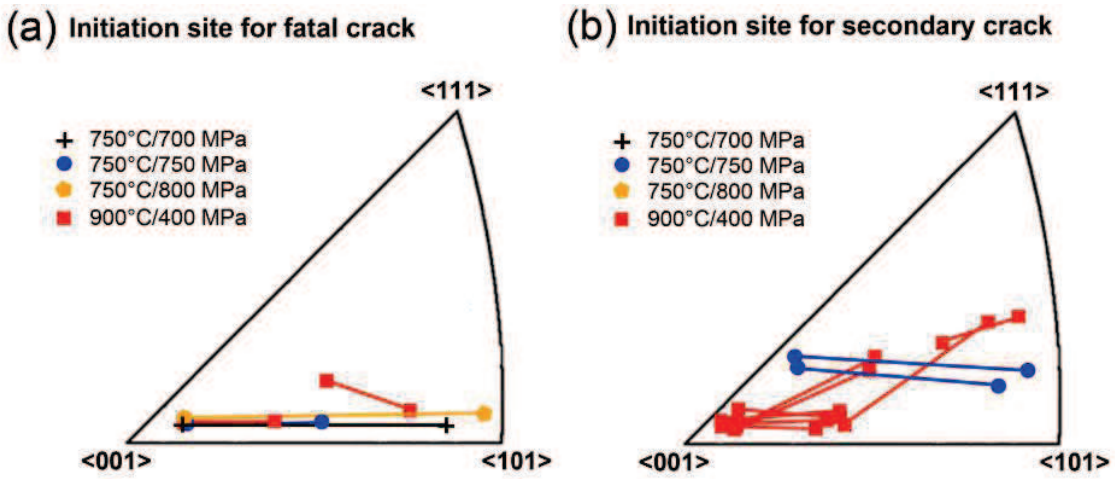

Figure 10: Grain boundary crystallographic configurations leading to fatal crack initiation (a) and to secondary crack initiation (b) in all DS200 investigated specimens. Primary and secondary initiation sites are grain boundaries that can be described by the two orientations along the loading direction of the grain they delimit.

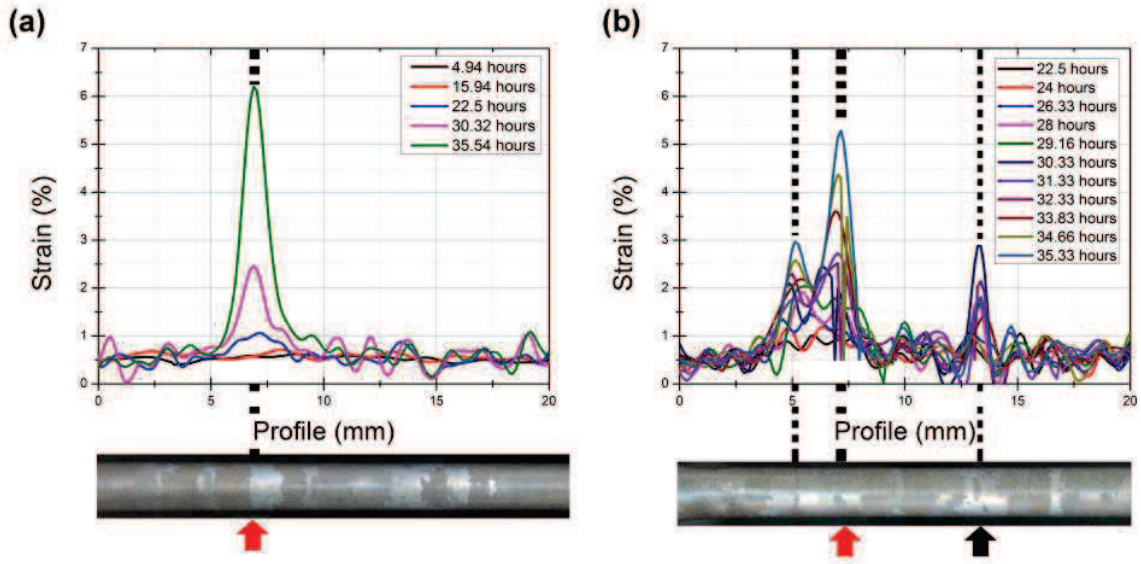

Figure 11: Local strain evolution followed by high temperature digital image correlation along two different profiles (along the gauge length) of a DS200 specimen during creep test at 740°C and 700 MPa. Red arrows points out at the fatal crack initiation site while the black arrow shows the location of a secondary crack initiation site.

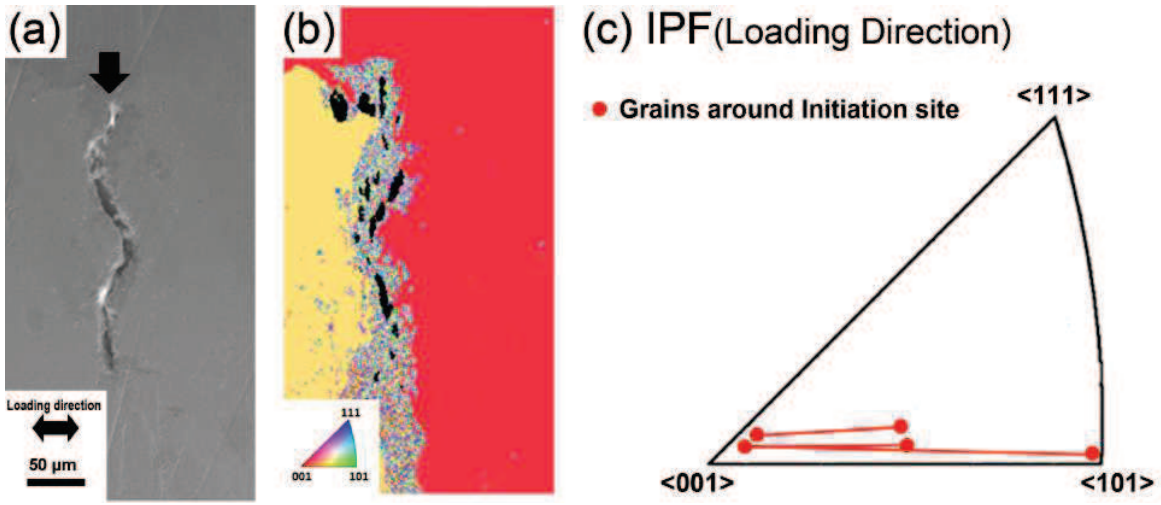

Figure 12: Grain boundary crystallographic configurations leading to crack initiation in a DS200 specimen tested at 740°C and 700 MPa. (a) Scanning electron microscope image of a secondary initiation site. (b) Associated EBSD map. Randomly oriented points in the vicinity of the crack are misindexed points and not associated with recrystallization events (c) Grain boundary crystallographic orientation leading to crack nucleation. Initiation sites are grain boundaries that can be described by the two orientations along the loading direction of the grain they delimit.

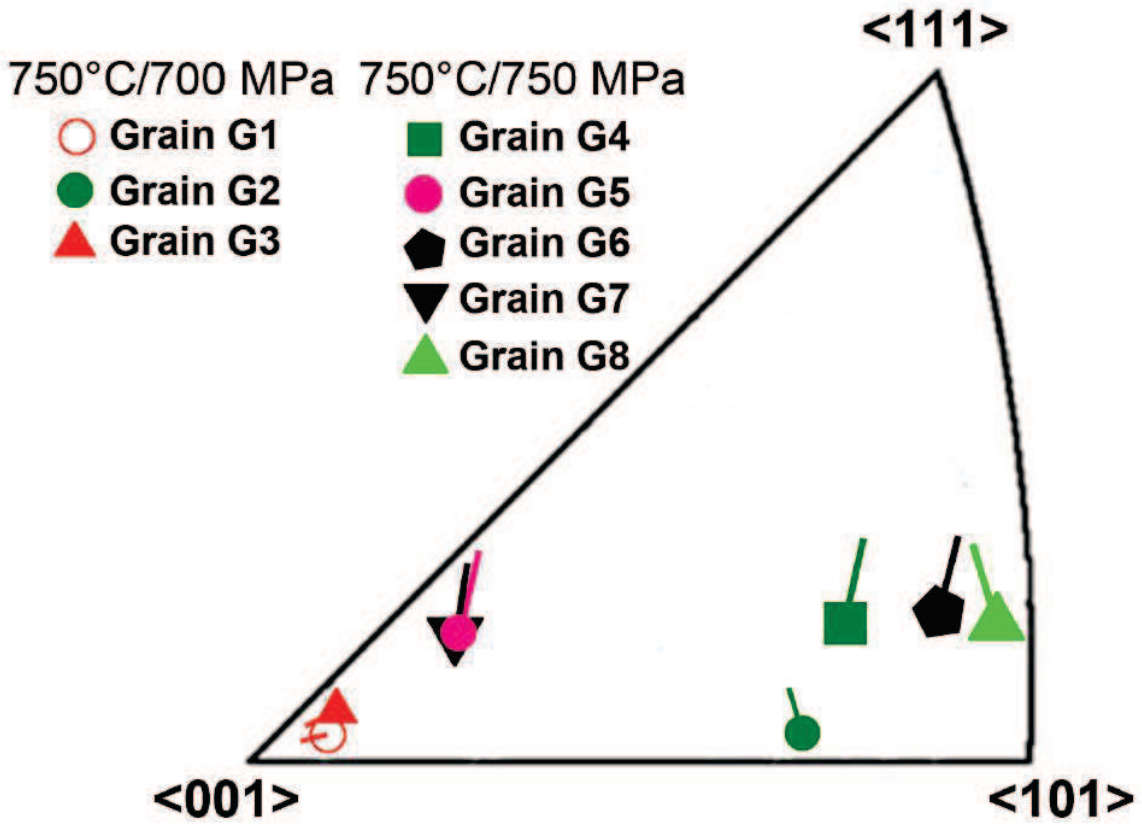

Figure 13: Evolution of the average crystallographic orientation per grain during creep test at 750°C and 700 MPa and 750°C and 750 MPa. Grain of interest labeled "G1" to "G8" as identified in Figure 8 are displayed in the inverse pole figure along the loading direction. The center of the symbols present the average orientation of the grain before creep test. The end of the lines present the average orientation of the grain after creep test.

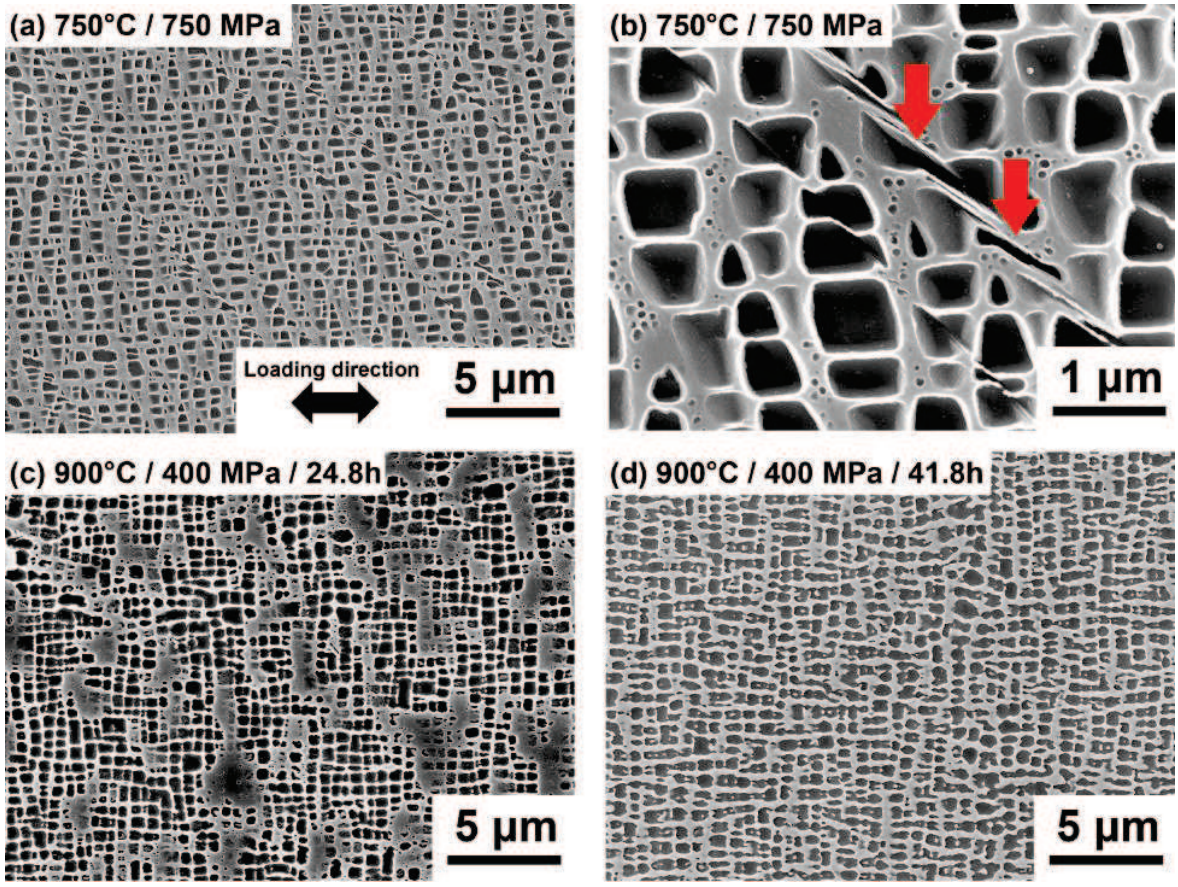

Figure 14: Evolution of the γ matrix and $\gamma\prime$ precipitates during creep tests at 750°C and 750 MPa (a-b) and 900°C and 400 MPa (c-d). (a-b) Scanning electron images after creep test at 750°C and 750 MPa significant $\gamma\prime$ precipitates shearing (red arrows). (c-d) Scanning electron images after interrupted creep test at 900°C and 400 MPa after 24.8 and 41.8 hours. Evidence of significant rafting and no $\gamma\prime$ precipitates shearing is observed.

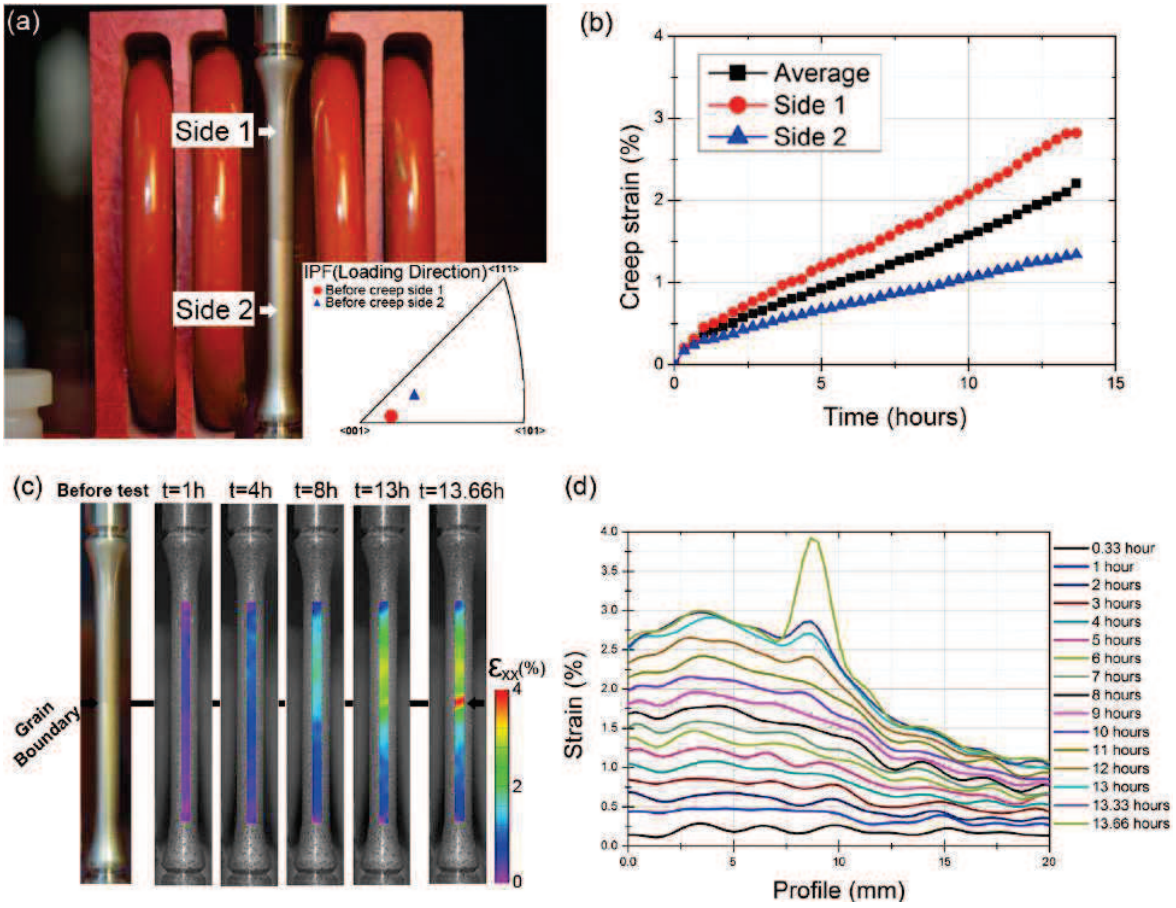

Figure 15: Creep test at 750°C and 700 MPa for a GTD444 bicrystal specimen (Figure 2(d)) and followed by digital image correlation measurements. (a) Optical image of the specimen showing the unique transverse grain boundary in the middle of the gauge length; The orientations of the grains on either sides of the boundary are given in insert using inverse pole figure along the loading direction. (b) Average strain evolution on either sides of the grain boundary during creep test. (c-d) The evolution of the local strain along the loading direction and across the gauge length as a function of time during creep test.

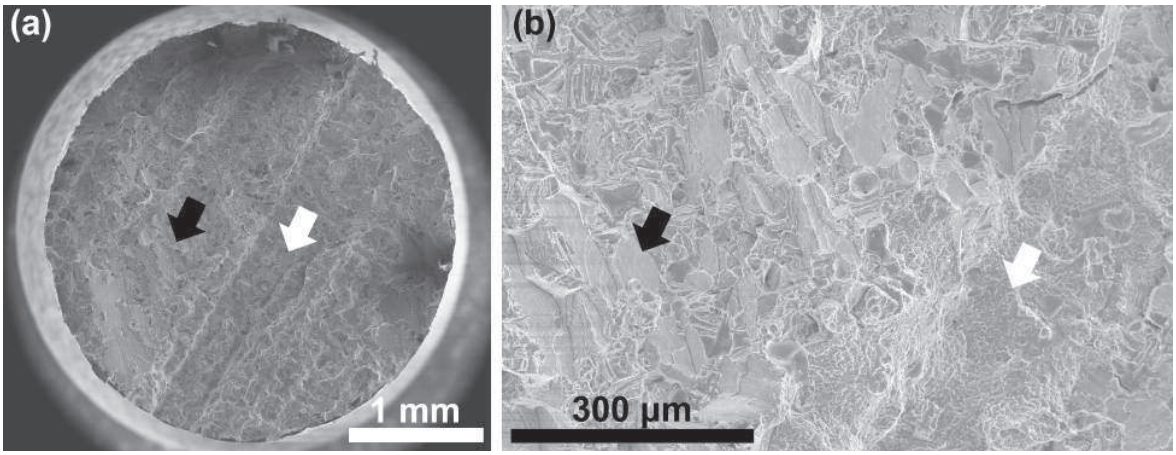

Figure 16: Fracture surface of a GTD444 bicrystal specimen tested at 750°C and 700 MPa showing signficant amount of intergranular (white arrows) and a relative amount of planar (black arrows) areas.

Declaration of interests

☒ The authors declare that they have no known competing financial interests or personal relationships that could have appeared to influence the work reported in this paper.

☐The authors declare the following financial interests/personal relationships which may be considered as potential competing interests:

NA